

# Quantification of CO<sub>2</sub> hotspot emissions from OCO-3 SAM CO<sub>2</sub> satellite images using deep learning methods

Joffrey Dumont Le Brazidec<sup>1</sup>, Pierre Vanderbecken<sup>1</sup>, Alban Farchi<sup>1</sup>, Grégoire Broquet<sup>2</sup>, Gerrit Kuhlmann<sup>3</sup>, and Marc Bocquet<sup>1</sup>

<sup>1</sup>CEREA, École des Ponts and EDF R&D, Île-de-France, France

<sup>2</sup>Laboratoire des Sciences du Climat et de l'Environnement, LSCE/IPSL, CEA-CNRS-UVSQ, Université Paris-Saclay, 91198 Gif-sur-Yvette, France

<sup>3</sup>Empa, Laboratory for Air Pollution / Environmental Technology, Dübendorf, Switzerland

**Correspondence:** Joffrey Dumont Le Brazidec - Current affiliation: European Centre for Medium-Range Weather Forecasts (ECMWF), Bonn, Germany (joffrey.dumont@ecmwf.int)

## Abstract.

This paper presents the development and application of a deep learning-based method for inverting CO<sub>2</sub> atmospheric plumes from power plants using satellite imagery of the CO<sub>2</sub> total column mixing ratios (XCO<sub>2</sub>). We present an end-to-end CNN approach, processing the satellite XCO<sub>2</sub> images to derive estimates of the power plant emissions, that is resilient to missing data in the images due to clouds or to the partial view of the plume due to the limited extent of the satellite swath.

The CNN is trained and validated exclusively on CO<sub>2</sub> simulations from 8 power plants in Germany in 2015. The evaluation on this synthetic dataset shows an excellent CNN performance with relative errors close to 20%, which is only significantly affected by substantial cloud cover. The method is then applied to 39 images of the XCO<sub>2</sub> plumes from 9 power plants, acquired by the Orbiting Carbon Observatory-3 Snapshot Area Maps (OCO3-SAMs), and the predictions are compared to average annual reported emissions. The results are very promising, showing a relative difference of the predictions to reported emissions only slightly higher than the relative error diagnosed from the experiments with synthetic images. Furthermore, the analysis of the area of the images in which the CNN-based inversion extract the information for the quantification of the emissions, based on integrated gradient techniques, demonstrates that the CNN effectively identifies the location of the plumes in the OCO-3 SAM images. This study demonstrates the feasibility of applying neural networks that have been trained on synthetic datasets for the inversion of atmospheric plumes in real satellite imagery of XCO<sub>2</sub>, and provides the tools for future applications.

## 1 Introduction

The satellite imagery of total column average dry air mole fraction of carbon dioxide (XCO<sub>2</sub>) from the Snapshot Area Map (SAM) mode of the Orbiting Carbon Observatory-3 (OCO-3) (Eldering et al., 2019) or the forthcoming CO2M mission (Janssens-Maenhout et al., 2020; Meijer et al., 2023) are pivotal for monitoring carbon dioxide (CO<sub>2</sub>) emissions. In the vicinity of large CO<sub>2</sub> anthropogenic sources, such as power plants, the satellite images may include CO<sub>2</sub> atmospheric plumes emanat-

ing from these sources. From these images, atmospheric inversion approaches can estimate the CO<sub>2</sub> emissions of the sources by analysing the signal intensity of the detected plumes (Nassar et al., 2017; Reuter et al., 2019; Chevallier et al., 2019; Wu et al., 2020; Zheng et al., 2020; Nassar et al., 2022; Chevallier et al., 2022; Cusworth et al., 2021).

25 Various approaches can be used to determine the emissions underlying the XCO<sub>2</sub> plumes in the satellite imagery. A first category rely on traditional atmospheric inversion methods that minimise the misfits between the satellite observations and simulations of the plumes with relatively expensive (Eulerian or Lagrangian) transport models to identify the optimal emission estimate (Pillai et al., 2016; Broquet et al., 2018). A second category are light-weight methods that apply the principle of mass conservation to compute the emissions from the CO<sub>2</sub> enhancement of the emission plume (such as integrated mass  
30 enhancements, divergence methods, and cross-sectional flux methods) or compare the observed plume with a Gaussian plume model (Gaussian plume inversions). Light-weight methods rely on wind fields taken, e.g., from meteorological reanalysis products. These light methods have been evaluated in several studies (e.g., Varon et al., 2018; Hakkarainen et al., 2024; Danjou et al., 2023; Santaren et al., 2024; Kuhlmann et al., 2024; Danjou et al., 2024). Despite the advancements in CO<sub>2</sub> plume inversion techniques, significant challenges remain, notably: 1) the extraction of plumes from XCO<sub>2</sub> backgrounds, hindered  
35 by low signal-to-noise ratios due to the large amplitude of background variations associated to the CO<sub>2</sub> natural fluxes, and to relatively large noise in the image (due to instrumental errors and to uncertainties in the retrieval of mole fractions from the satellite measurements), (2) the complex process of deducing the source emissions from clearly delineated plumes, marred by uncertainties in the corresponding transport and dispersion (i.e., in either the transport modelling or in the wind field and assumptions regarding the vertical structure of the 3D CO<sub>2</sub> plume for the derivation of the effective wind driving the 2D XCO<sub>2</sub>  
40 plume in the light-weight analysis (Dumont Le Brazidec et al., 2022), and (3) reconstructing emissions from images with a partial view of the plumes due to missing data where there are clouds or gaps in satellite coverage.

Machine learning models have been suggested in response to these obstacles and have been primarily applied to CH<sub>4</sub> and NO<sub>2</sub> images (e.g., Lary et al., 2016; Finch et al., 2021; Jongaramrungruang et al., 2021; Joyce et al., 2023; Kumar et al., 2023). Our previous work (Dumont Le Brazidec et al., 2022, 2023) pioneered the use of deep learning methodologies, specifically  
45 Convolutional Neural Networks (CNNs), for the segmentation and inversion of CO<sub>2</sub> plumes for the estimate of point sources. This approach has demonstrated its efficacy in addressing these challenges when tackling synthetic satellite image with a full coverage of the plumes, i.e. without the loss of observations due to cloud cover or quality control in the satellite limited field of view. This paper is a direct continuation of Dumont Le Brazidec et al. (2023). Specifically, our approach involves developing a supervised learning CNN system designed to predict CO<sub>2</sub> emissions using XCO<sub>2</sub> images and ancillary data (such as wind  
50 fields, time, and NO<sub>2</sub> images which will be measured by CO2M). This CNN is trained on a synthetic dataset, constructed from model simulations, comprising synthetic XCO<sub>2</sub> fields and the corresponding true emissions. Through this training process, the CNN learns to correlate specific features within the input images covering the plume from a targeted point source with certain output values, namely the emissions from the point source. The CNN's capability to generalise is subsequently assessed using a new, unseen dataset during the training phase. In particular, this assessment is based on tests targeting a source which was  
55 not covered by the synthetic images used for the training phase.

Our previous research (Dumont Le Brazidec et al., 2022) evaluated the models using only synthetic images without missing data, comparing them against light alternative methods where they demonstrated better performance with an absolute error about half of that of the cross-sectional flux method. In the current study, we extend our approach by analysing actual satellite data, specifically examining 39 OCO-3 SAM observations to quantify emissions. Those images of  $64\text{km}^2$  cover 9 power plants located in the USA (7), Europe (1), and China (1). To make this possible, this paper introduces a new upgrade of the CNN approach to address the third principal challenge in  $\text{CO}_2$  plume inversion: handling images with a partial cover of the plumes due to the loss of observations associated to clouds, or due to the limited extent of the satellite swath. Furthermore, the training of the CNN involves a novel data augmentation strategy, specifically the incorporation of beta or uniform distribution mappings for plumes and the corresponding emissions. This enhancement aims to improve the robustness and stability of the CNN in predicting  $\text{CO}_2$  emissions under various conditions.

The structure of this paper is as follows: Section 2 introduces the synthetic dataset, which bears significant resemblance to the one described by Dumont Le Brazidec et al. (2023) and Santaren et al. (2024), the OCO-3 SAMs utilised exclusively for evaluation, and the dataset’s training/validation/test split strategy. Section 3 details the model, the developed data augmentation approach aimed at stabilising CNN training, the methodology for addressing the problem of clouds, and the training parameterisation. In Section 4, we successively present the CNN’s emission estimations for plumes across the synthetic and OCO-3 SAM datasets. Special attention is given to analysing the model’s OCO-3 SAM predictions through the lens of integrated gradients, a method that elucidates the contribution of each input feature to the model’s predictions, enhancing interpretability. Finally, Section 5 discusses cogent future directions, before we conclude.

## 2 Dataset

### 2.1 Synthetic dataset

The synthetic dataset employed in this study is very similar to the one used by Dumont Le Brazidec et al. (2023). The dataset consists of hourly  $\text{XCO}_2$  and  $\text{NO}_2$  fields from the SMARTCARB project (Brunner et al., 2019; Kuhlmann et al., 2019), which generated one year of synthetic  $\text{CO}_2$  observations from high-resolution  $\text{CO}_2$  and  $\text{NO}_2$  transport simulations covering power plants in Germany, Poland and the Czech Republic. The SMARTCARB dataset has been used in various studies for assessing emission quantification methods (e.g., Kuhlmann et al., 2020, 2021; Hakkarainen et al., 2021; Santaren et al., 2024). For this study, we extracted  $32 \times 32$  pixel ( $2\text{km}$  resolution) fields centred around different power plants. For comparison, in Dumont Le Brazidec et al. (2023), the image size was chosen as  $64 \times 64$ . The transition to focusing analysis on a more confined area surrounding the hotspots (power plants) is driven by several factors: i) the critical portion of the plume influencing emission reconstruction typically lies within this central area, as noted in Dumont Le Brazidec et al. (2023), ii) satellite swath limitations - the limited spatial extent of a swath and temporal constraints between two swaths makes it unlikely that satellite imaging will consistently capture  $128\text{ km}^2$  areas centred over emission sources, and iii) this more focused approach demonstrates a stabilising effect on neural network training, likely due to the reduction of superfluous information.

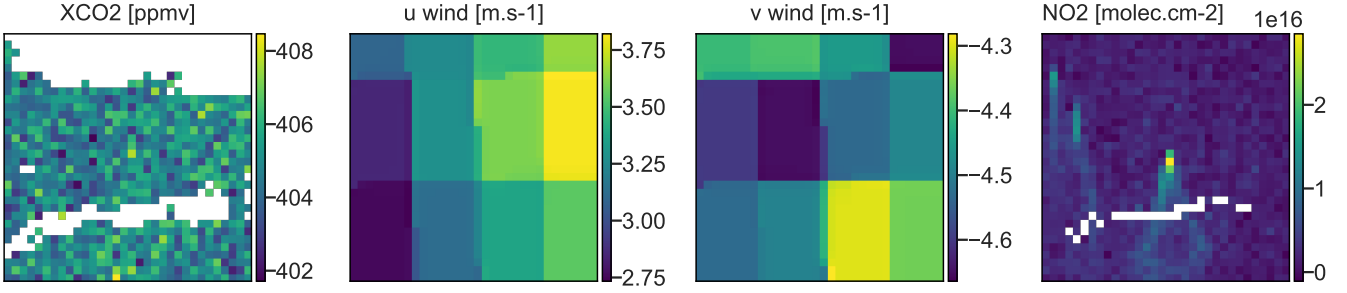


**Figure 1.** Examples of inputs used by the CNN model. The first, second, third and fourth columns represent the XCO<sub>2</sub> images, vertically averaged  $u$  and  $v$  winds, and NO<sub>2</sub> images, respectively. The power plant of interest is always located in the middle of the image.

To account for the inherent noise of satellite instruments, we introduce Gaussian random noise with a standard deviation of 0.7ppm to the XCO<sub>2</sub> images, reflecting typical noise levels expected for OCO-3 and CO<sub>2</sub>M snapshots as reported by Meijer (2020); Taylor et al. (2023); Danjou et al. (2024). Given the observed strong correlation between NO<sub>2</sub> and CO<sub>2</sub> plumes and CO<sub>2</sub>M’s capability to measure NO<sub>2</sub>, we incorporate noisy NO<sub>2</sub> fields in our analysis, characterised by Gaussian noise with a variance of  $1e15 \text{ molec.cm}^{-2}$  (Kuhlmann et al., 2019).

Similarly to Dumont Le Brazidec et al. (2023), we integrate ERA5 wind data as additional inputs to the CNN model, aligning its original resolution of 28 km with the 2 km resolution used for the CO<sub>2</sub> and NO<sub>2</sub> images. Specifically, we employ 2D  $u$  and  $v$  wind fields, representing the average zonal and meridional winds, respectively, across the five lowest model levels of ERA5. This averaging process approximates the atmospheric conditions below 100 m.

To include the impact of cloud cover in the inversion of CO<sub>2</sub> plumes, we use the simulated cloud cover fractions extracted from the SMARTCARB dataset to mask pixels where retrievals are not available due to high cloud fraction. Following Kuhlmann et al. (2019), we use a cloud threshold of 1% for CO<sub>2</sub> images and 30% for NO<sub>2</sub> images.

Moreover, we study the interest of introducing temporal information to our CNN inputs, by incorporating the hour of the day, day of the week, and day of the year. To capture the cyclical nature of time, these features are transformed into cosine and sine representations, ensuring proximity between temporally adjacent data points (e.g., the last and first hours of the day). Consequently, each XCO<sub>2</sub> field is associated with a vector of six scalar values encoding the temporal context of the observation. In Fig. 1, we present a typical input data used by the CNN to predict the emissions of the local hotspot.

## 2.2 Set of OCO-3 SAMs

The OCO-3 SAM mode is an observation strategy designed to monitor CO<sub>2</sub> emissions from specific emission hotspots (large urban areas and large industrial point sources). Unlike its standard observation mode, which conducts continuous scans of the Earth’s atmosphere in nadir or glint mode, the SAM mode is a targeting mode, which provides high-resolution XCO<sub>2</sub> images around such emission hotspots. In this study, we have selected 39 OCO-3 SAMs at nine power plants to evaluate the applicability and reliability of our CNN model trained on synthetic datasets. We selected OCO-3 SAM images corresponding

Power plant	Coordinates [°N, °E]	Reported emissions [Mt CO <sub>2</sub> /a]	Number of OCO-3 images
Colstrip	[45.88, -106.61]	13.6	4
Belchatow	[51.27, 19.33]	37.6	4
Tuocketuo	[40.20, 111.36]	29.5	8
Cumberland	[36.39, -87.65]	12.4	3
Labadie	[38.56, -90.84]	15.0	6
Intermountain	[39.51, -112.58]	5.0	2
Hunters	[39.17, -111.03]	7.2	7
Parish	[29.48, -95.63]	13.2	4
Conemaugh	[40.38, -79.06]	16.9	1

**Table 1.** List of power plants selected for this study, along with their annual reported emissions, coordinates, and number of observations used. The data spans from 2020 to 2023. Emissions statistics are sourced by (Nassar et al., 2021; Grant et al., 2021; Lin et al., 2023) which are based on the US Environmental Protection Agency (EPA) (<https://www.epa.gov/airmarkets/power-sector-emissions-data>) and the European Pollutant Release and Transfer Register (E-PRTR, <https://prtr.eea.europa.eu>).

to power plants for which reports of the emissions are available and have been studied in the scientific literature, and to a sufficient number of cloud-free XCO<sub>2</sub> retrievals of good quality. The list of power plants selected are described with average reported emission and number of collected SAMs in Table 1.

To adapt the raw OCO-3 SAM data for CNN analysis, we first construct a 32×32 grid with a resolution of 2 km (similar to the resolution of OCO3-SAM or CO2M) and centred at the power plant. Each grid cell is populated through a weighted interpolation of surrounding OCO-3 SAM data pixel centers, considering only those within a distance of less than 0.66 times the new grid resolution. This specific distance threshold was determined through experimentation to optimally preserve information from the original dataset. Although this mapping strategy provides a straightforward means of converting OCO-3 SAM data into a format compatible with our CNN, it is acknowledged that this approach has limitations and the observation information might not be perfectly conserved. Additionally, since most OCO3-SAM snapshots used in this study were taken in 2021 or 2022, the synthetic images are adjusted to account for the effect of climate change and the general increase of 2.3ppm per year in CO<sub>2</sub> concentration since 2015 (SMARTCARB synthetic dataset year). Figure 2 illustrates with 8 examples the process of transforming original OCO-3 SAM data into an XCO<sub>2</sub> field suitable for CNN reconstruction.

### 2.3 Training, validation, and test split choices

For tests on synthetic and real data, a rigorous geographical separation is maintained between the power plants used in the training and validation datasets and those in the test dataset to avoid data leakage. For instance, when training a model to predict emissions from the Boxberg power plant, Boxberg plumes are excluded from the training set. The validation dataset

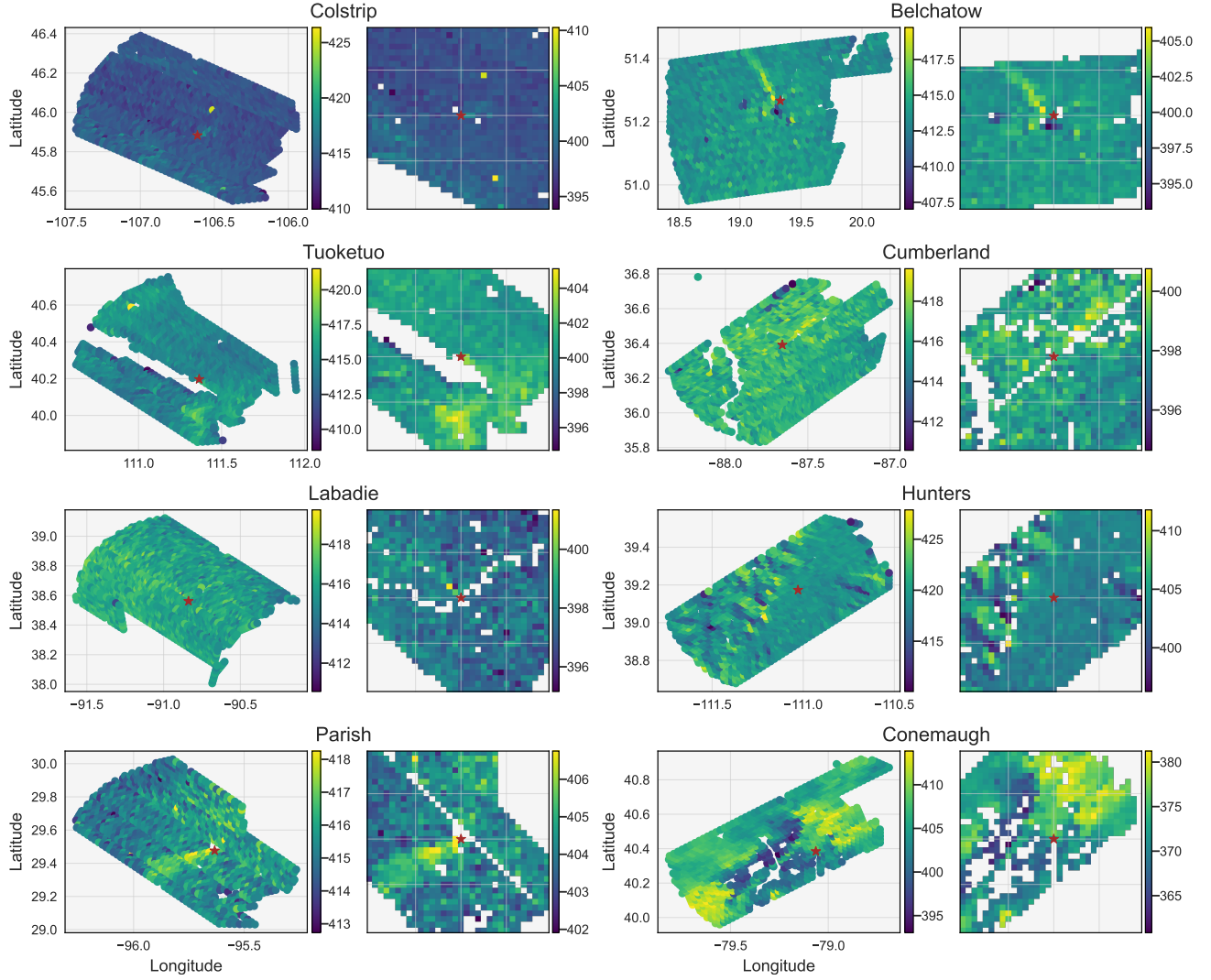


**Figure 2.** Examples of OCO-3 SAM observations for eight different power plant and their transformation into CNN-compatible images. For each case, on the left is described the original OCO-3 SAM data and on the right the corresponding CNN-compatible mapping (for which the power plant is always at the centre of the image). All values are in ppmv.

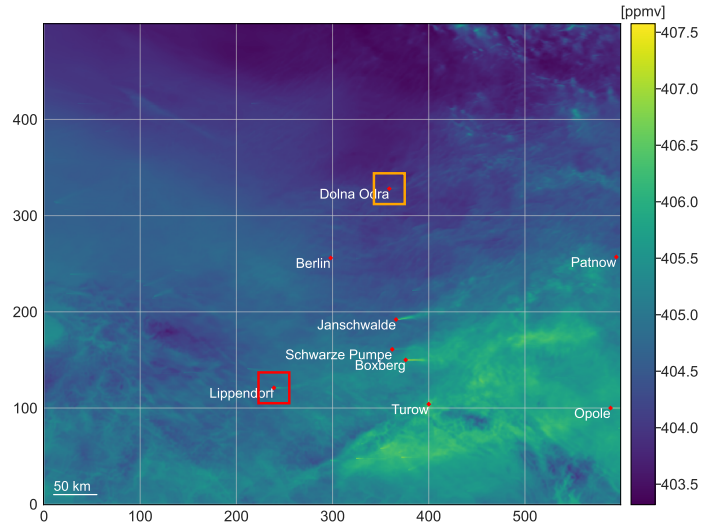


**Figure 3.** Map of XCO<sub>2</sub> concentrations within the complete SMARTCARB domain on 12 December 2015 at 03:00 UTC. The depicted XCO<sub>2</sub> fields are devoid of synthetic satellite noise for visibility. When constructing a model to predict emissions from Lippendorf, based on Lippendorf-centred fields (indicated by the red square), images from Dolna Odra (indicated by the orange square) are used for validation, whereas images from the remaining power plants serve as training data.

comprises plumes from a different power plant, Dolna Odra, which is neither used to train nor test the CNNs. This splitting strategy is exposed in Fig. 3.

130 This approach mirrors the strategy adopted in Dumont Le Brazidec et al. (2023) for analysis on synthetic images. We focus on the same three power plants for the tests: Lippendorf, Boxberg, and Turow, training distinct models for each to predict their emissions. These models share the same architectural framework, hyperparameters, CNN structure, and preprocessing layers, but are trained on a dataset excluding plumes from its target power plant.

The rationale behind selecting Lippendorf, Boxberg, and Turow as test power plants is thoroughly discussed by Dumont  
 135 Le Brazidec et al. (2023). Briefly, these power plants were chosen for their distinct characteristics: Lippendorf averaged emissions are equal to 15.2 Mt CO<sub>2</sub>/yr; Boxberg’s plume is often located close to other power plant plumes and its average emissions amount to 19.0 Mt CO<sub>2</sub>/yr ; and Turow is characterised by low emissions of 8.7 Mt CO<sub>2</sub>/yr. This selection criteria ensures an evaluation of the proposed CNN architecture across various emission scenarios.

It is critical to underline that while the test dataset for one experiment becomes part of the training dataset for another, each  
 140 experiment was conducted independently, ensuring that model tuning was not optimised by outcomes derived from the test datasets. Finally, in our assessment of CNNs against OCO-3 SAM data, the training was based exclusively on synthetic data.

### 3 Deep learning methodology

The goal of this study is to determine the CO<sub>2</sub> emission rate (in MtCO<sub>2</sub>.yr<sup>-1</sup>) of the hotspot in the center of a XCO<sub>2</sub> image using a CNN model, which takes the XCO<sub>2</sub> image alongside other data as input. This section describes the CNN model and the data augmentation strategy, with a particular focus on the method to address cloud interference, and discusses training parameters.

#### 3.1 CNN model and preprocessing layers

This subsection describes the CNN-based inversion system (the CNN model with its preprocessing layers that estimates emissions from images) and how it is trained. The CNN-based inversion system is a compound of preprocessing layers and a core CNN model. Preprocessing layers are operations successively applied to the XCO<sub>2</sub> fields and ancillary data before they are processed by the core CNN model. The core CNN model is a statistical model whose parameters (or neurons) are optimised during the training phase: its function is to identify and extract features from the input data, which it learns to associate with specific levels of emissions. The training phase of the CNN-based inversion system consists in a series of five steps, depicted in Fig. 4 and in the following paragraphs.

##### 3.1.1 Data augmentation

The data augmentation process creates an artificially infinite dataset from the SMARTCARB dataset to prevent the model from overfitting due to the SMARTCARB dataset's limitations. Specifically, instead of using XCO<sub>2</sub> field directly from the SMARTCARB dataset to train the core model, we use a composition of five different elements:

1. The principal component is a synthetic image centred on a major power plant of interest, exclusively containing the XCO<sub>2</sub> plume from that facility and the other major power plants. The SMARTCARB dataset composition facilitates isolating this field from all other anthropogenic and biogenic fluxes. This first component undergoes a distribution mapping: an emission level is randomly drawn from a probability distribution, either a beta (to mitigate the training on extreme emissions) or a uniform as shown in Fig. 5, and the plume image is adjusted accordingly (we trained separate CNN models for each distribution choice).  
Simultaneously, the CNN output is also adjusted at the emission level.
2. To this first component is added a randomly drawn XCO<sub>2</sub> background, which is augmented by summing it with a random number  $b \sim U(-3.5, 3.5)$  (in ppmv), added uniformly across the field, in a manner analogous to Dumont Le Brazidec et al. (2023). The selection of the background (and all subsequently described elements) through uniform random drawing is independent from the position of the main plume component.
3. To this is added other anthropogenic XCO<sub>2</sub> plumes identified in the SMARTCARB area, each scaled by a random factor ranging from 0.33 to 3.



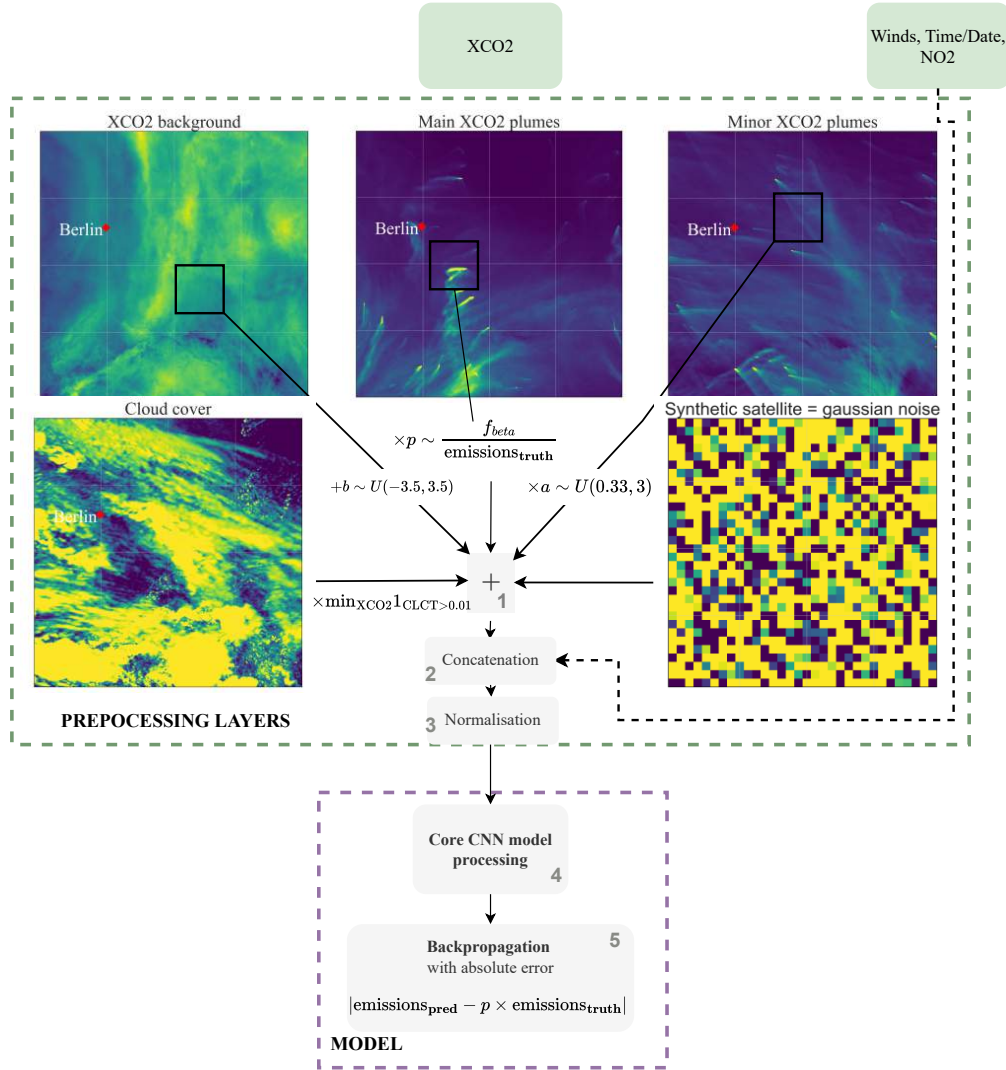


**Figure 4.** Description of the inversion system at training time as a compound of preprocessing layers and the model. The CNN-based inversion system consists in five steps: 1) construction of an XCO<sub>2</sub> field as a sum of background XCO<sub>2</sub>, major and minor CO<sub>2</sub> plumes, cloud cover and synthetic satellite noise, represented by gaussian noise with a standard deviation of 0.7 ppmv and zero mean. The major plumes are scaled using either a beta or uniform distribution (with only the beta distribution shown in the Figure), a uniform random field between -3.5 and 3.5 ppmv is added to the background, and the remaining plumes are scaled by random factors drawn from a uniform distribution between 0.33 and 3. Pixels in the reconstructed XCO<sub>2</sub> field are marked as missing (nan) when cloud coverage exceeds a specified threshold. The plumes of interest are augmented by a beta or uniform distribution (only beta is represented on the Figure), the background is added to uniformly drawn fields between -3.5 and 3.5 ppmv, the other plumes are multiplied with a uniform distribution between 0.33 and 3. The reconstructed XCO<sub>2</sub> field pixels are considered as nan or not according to the clouds according to a given threshold. 2) concatenation with ancillary data (winds, time, and NO<sub>2</sub>), 3) standardisation of the fields, 4) processing by the core CNN model, and 5) and backpropagation.

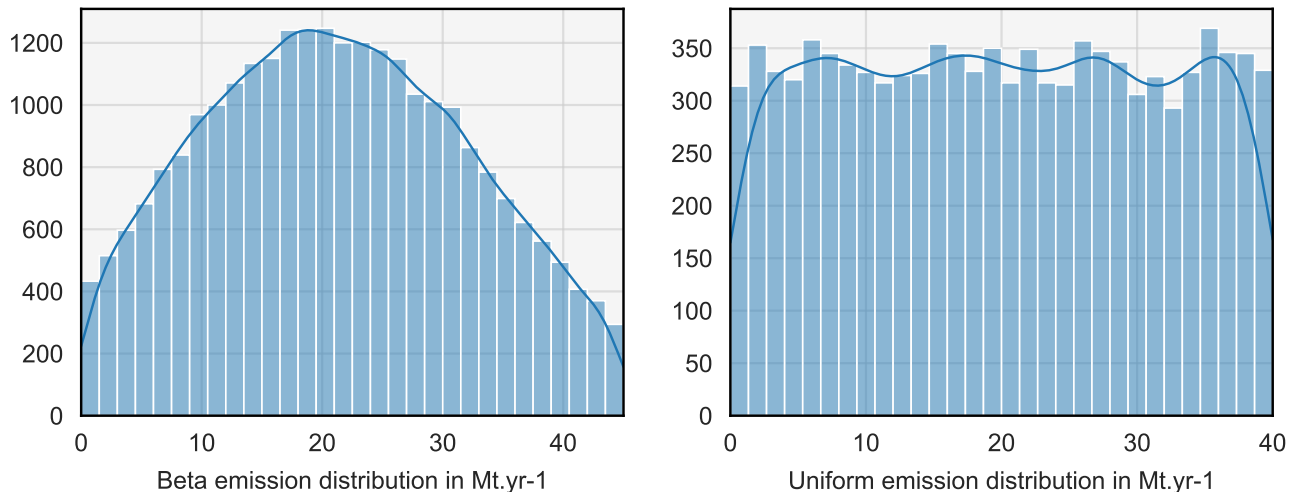


**Figure 5.** At training time, the hotspot emission and corresponding plume are adjusted based on a random draw from either a beta or uniform distribution.

4. The application of cloud cover constitutes the fourth component. A random selection of cloud cover from the SMART-CARB area is made, independent from the selections for other fields. XCO<sub>2</sub> pixels are deemed unobserved when cloud cover exceeds 0.01, leading to replacement with NaN, which are subsequently replaced with the minimum value across all XCO<sub>2</sub> fields. This is meant for the CNN model to learn to ignore this non-informative constant value.

5. The fifth component adds to the other fields random Gaussian noise with a variance of 0.7 ppmv.

### 3.1.2 Concatenation

The concatenation of the main XCO<sub>2</sub> field with the ancillary data represents the second step. The ancillary data may include wind conditions, the time and date of the observation, and the NO<sub>2</sub> field. In instances where the NO<sub>2</sub> field is incorporated, it also undergoes a data augmentation process (not depicted in Figure 4). Initially, the NO<sub>2</sub> plume is scaled by a random factor drawn from a uniform distribution ranging from 0.75 to 2 to ensure the NO<sub>2</sub> plume amplitude are decorrelated from that of the CO<sub>2</sub> plume, thus preventing the core CNN model from relying for inversion on the tight correlation between the NO<sub>x</sub> and CO<sub>2</sub> emissions. In principle, due to the large variations and uncertainties in the CO<sub>2</sub>-to-NO<sub>x</sub> emission and lifetime of NO<sub>x</sub>, NO<sub>2</sub> should primarily support the plume detection in the overall inversion process. Subsequently, the NO<sub>2</sub> field is partially masked due to cloud coverage. For this, we adopt the criterion from Kuhlmann et al. (2019) that an NO<sub>2</sub> pixel is marked as NaN if its cloud coverage fraction exceeds 0.3. Furthermore, the NO<sub>2</sub> field is subject to Gaussian noise with a variance of  $1 \times 10^{15}$  molecules.cm<sup>-2</sup> (Kuhlmann et al., 2019).

### 3.1.3 Normalisation

Z-score normalisation of each physical field within the concatenated input data constitutes the third step, performed independently for each channel.

### 3.1.4 Processing

The fourth step is the core CNN model mapping from  $\text{XCO}_2$  and ancillary fields to a scalar emission value. This model, consistent with the one described in Dumont Le Brazidec et al. (2023), features a series of convolutional, max pooling, batch normalisation, and dropout layers, with a total of 186,000 trainable parameters. Specifically, if time and date features are used, they are integrated into the CNN post feature extraction (following the last dense layer).

### 3.1.5 Backpropagation

The final step entails computing the loss gradient, enabling neuron adjustments within the core CNN model through backpropagation.

In contrast to the training phase, the inversion system at evaluation phase consists only in the concatenation, normalisation, and processing by the core CNN model. The synthetic test dataset consists in pre-constructed, physically consistent simulated data (except for clouds as explained in Section 3.2), maintaining consistency with the methodology outlined in Dumont Le Brazidec et al. (2023).

## 3.2 Clouds

To assess the impact of cloud cover on CNN performance, we consider models trained and tested on varied datasets distinguished by varying degrees of fraction of cloudy pixels in the  $\text{XCO}_2$  images:

- A first series of models are trained and tested on  $\text{XCO}_2$  images under clear-sky conditions.
- A second series of models are trained and tested on  $\text{XCO}_2$  images with cloud coverage ranging from 0% to 25%.
- A third series of models are trained on  $\text{XCO}_2$  images with cloud coverage from 0% to 50% but are tested on images with cloud coverage from 25% to 50%.
- A final series of models are trained on  $\text{XCO}_2$  images with cloud coverage from 0% to 75% but are tested on images with cloud coverage from 50% to 75%.

These varying degrees of cloud coverage are constructed through random sampling of cloud coverage over the SMARTCARB domain. This method of training and testing models under varying cloud conditions allows us to compare the degradation in model performance with increased cloud coverage. Additionally, training the model tested on cloud coverage between 50% and 75% on a range from 0% to 75% ensures the maintenance of a "universal" model capable of inverting plumes in scenarios with both low and high cloud coverage.

Power plant	with NO <sub>2</sub>	cloud fraction			
		0	0 to 25%	25 to 50%	50 to 75%
<b>Lippendorf</b>	<b>✗</b>	23.1	22.8	25.1	23.7
<b>Lippendorf</b>	<b>✓</b>	17.9	18.7	21.6	23.5
<b>Boxberg</b>	<b>✗</b>	18.5	19.5	20.2	21.1
<b>Boxberg</b>	<b>✓</b>	15.6	15.5	16.7	19.5
<b>Turow</b>	<b>✗</b>	35.8	35.4	37.6	57.3
<b>Turow</b>	<b>✓</b>	24.8	28.9	37.9	65.2

**Table 2.** Median of the relative error between the CNN predictions and the true emissions for Lippendorf, Boxberg, Turow, for varying levels of clouds and input configurations. Entries in the table represent relative errors expressed as percentages of the true emissions.

### 3.3 Training parameterisation

We configure the training hyperparameters as follows: the model uses the Adam optimiser, with an initial learning rate of  $1 \times 10^{-3}$ , which is adjusted according to a reduce-on-plateau strategy down to  $1 \times 10^{-5}$  with a patience parameter set to 20. The batch size is established at 128, and the training process spans 750 epochs. These parameters were selected based on a rigorous experimental process, combined with adherence to established practices in the field. For the loss function, the Mean Absolute Error (MAE) was chosen.

## 4 Application to synthetic and OCO-3 SAM observations

### 4.1 Application to synthetic dataset

Similarly to Dumont Le Brazidec et al. (2023), we investigate the performance of various CNN models in predicting the emissions of the Lippendorf, Turow, or Boxberg power plants. A collection of CNNs undergoes training on subsets of power plants, each excluding one for evaluation. For each power plant, a collection corresponds to models that are trained and tested on images affected by varying levels of cloud coverage. In addition, the models are trained with two different input configurations: one that includes XCO<sub>2</sub>, wind, time, and NO<sub>2</sub> data, and another that includes all these variables except for NO<sub>2</sub>. As a result, a total of 3 (number of target power plants)  $\times$  4 (cloud coverage scenarios)  $\times$  2 (input configurations) = 24 CNNs are trained and evaluated.

Figures 6 and 7 show Kernel Density Estimation (KDE) plots for the absolute relative error and the algebraic difference between the model predictions and the true emissions for the configuration without and with NO<sub>2</sub> input. A comprehensive summary of the results is also provided in Table 2.

The novel data augmentation strategy presented in Section 3.1 improves the stability of the performances of the CNNs in comparison to Dumont Le Brazidec et al. (2023), making it unnecessary to train a CNN ensemble to achieve satisfactory and

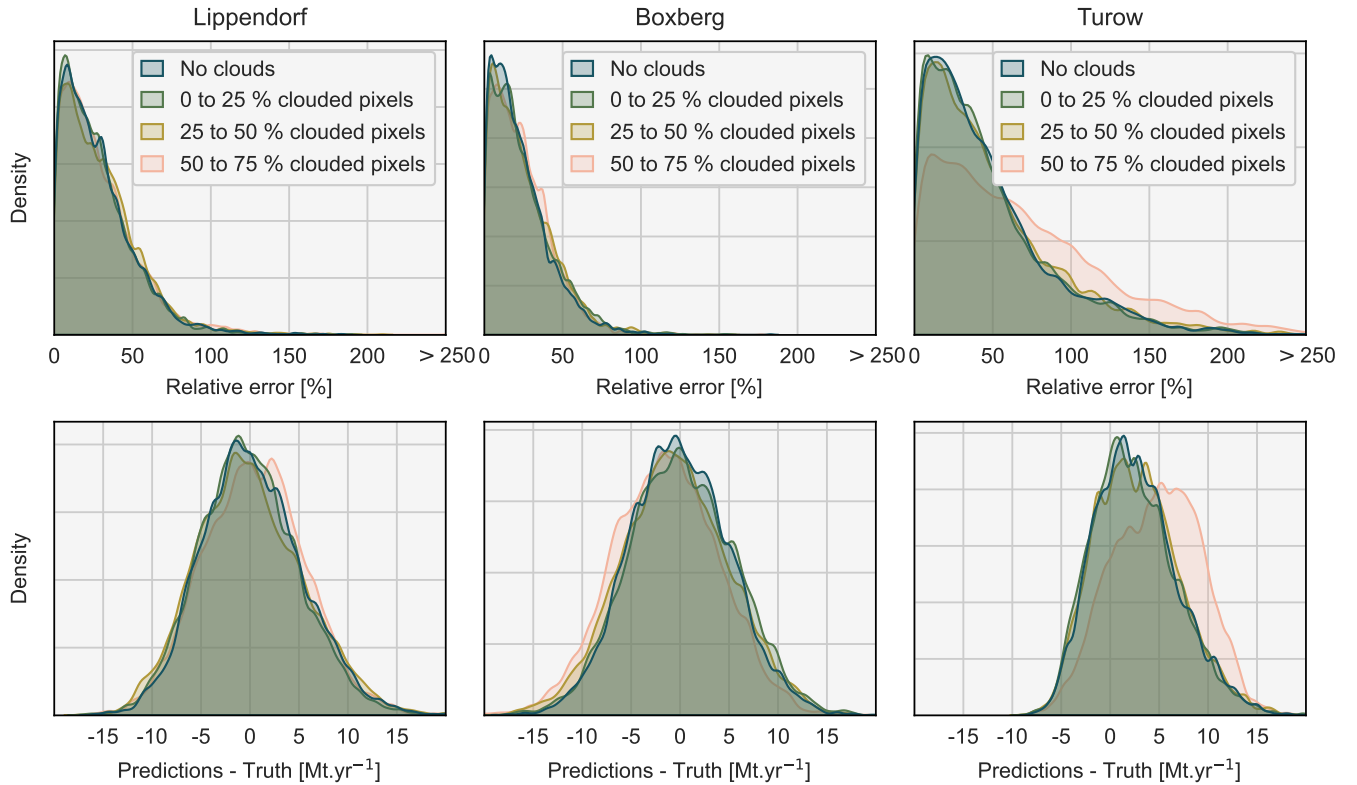


**Figure 6.** Density plots of the absolute relative error and of the algebraic difference between the CNN predictions and the reported emissions. The CNN models are trained and evaluated with XCO<sub>2</sub>, wind, and time input data, affected by varying levels of cloud coverage. Predictions with absolute relative errors greater than 250% or absolute errors greater than 15 Mt.yr<sup>-1</sup> were set to 250 or 15 to increase visibility.

consistent results. Significantly, in comparison to Dumont Le Brazidec et al. (2023), Boxberg median relative error with NO<sub>2</sub> decreased from 36.9% to 15.6%. Furthermore, (not shown) an improvement in the results is observed when using the mean of the emissions predicted by applying the CNN to an ensemble of images with added Gaussian noise. Specifically, for added  
240 Gaussian noise with a standard deviation of 0.3, the Lippendorf median relative error (without additional inputs) decreases from 23.1% to 18.5%. Finally, incorporating time or wind as a feature yields no significant benefit in the performance of the CNNs.

Concerning the influence of clouds, in the cases of Lippendorf and Boxberg, the accuracy of plume emission predictions is not significantly compromised by their introduction, even with high cloud coverage exceeding 50%. This observation is valid  
245 whether or not NO<sub>2</sub> is factored into the analysis. However, for Turow, a power plant with lower emissions, the performance of CNN predictions degrades progressively with an increase in cloud coverage, notably when cloud coverage exceeds 50%. The specific decline in prediction accuracy for Turow can likely be traced back to the fact that the Turow's plume is mostly indistinguishable from the background. Consequently, the CNN's capacity to accurately estimate Turow's emissions is inherently

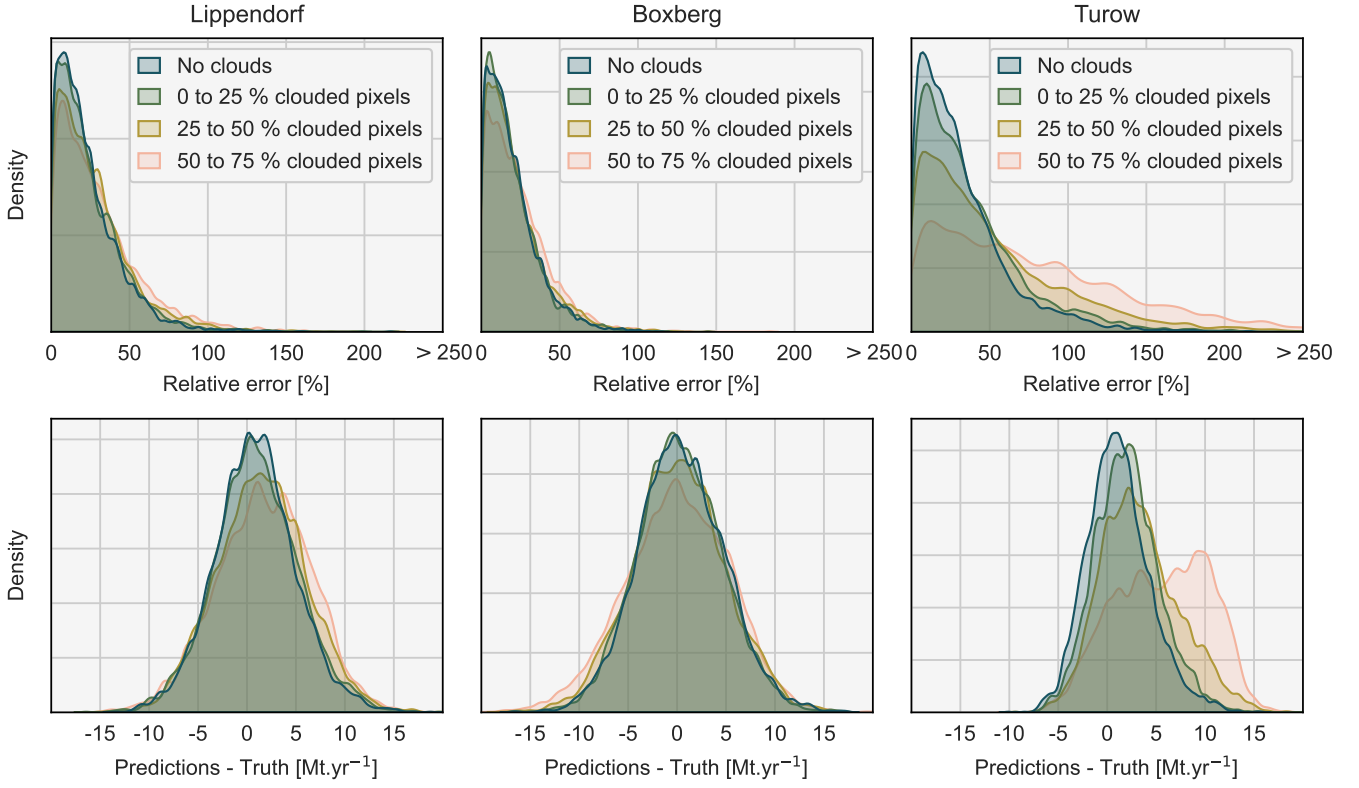


**Figure 7.** Density plots of the absolute relative error and of the algebraic difference between the CNN predictions and the reported emissions. The CNN models are trained and evaluated with  $\text{XCO}_2$ , wind, time, and  $\text{NO}_2$  input data, affected by varying levels of cloud coverage. Predictions with absolute relative errors greater than 250% or absolute errors greater than  $15 \text{ Mt.yr}^{-1}$  were set to 250 or 15 to increase visibility.

based on limited information, even in the absence of clouds. The introduction of cloud cover exacerbates this issue by further  
250 diminishing the available information.

## 4.2 Application to OCO-3 SAM observations

In this section, we assess the ability of CNNs trained on power plant plumes from the SMARTCARB synthetic dataset encompassing the power plants of Janschwalde, Schwarze Pumpe, Boxberg, Lippendorf, Turow, Patnow, and Opole, to estimate emissions from real plumes observed at power plants by OCO-3 SAM, along with ERA5 wind fields and time information. A  
255 total of 39 observations of OCO-3 SAM data for 9 power plants are examined.

To obtain meaningful statistics from the small number of images, we use two different methods to increase the number of predictions for each image:

1. An ensemble of 100 images  $x_i^1, \dots, x_i^{100}$  for each normalised OCO-3 SAM observation  $x_i$ , where  $x_i^j \sim \mathcal{N}(x_i, 0.3)$ .

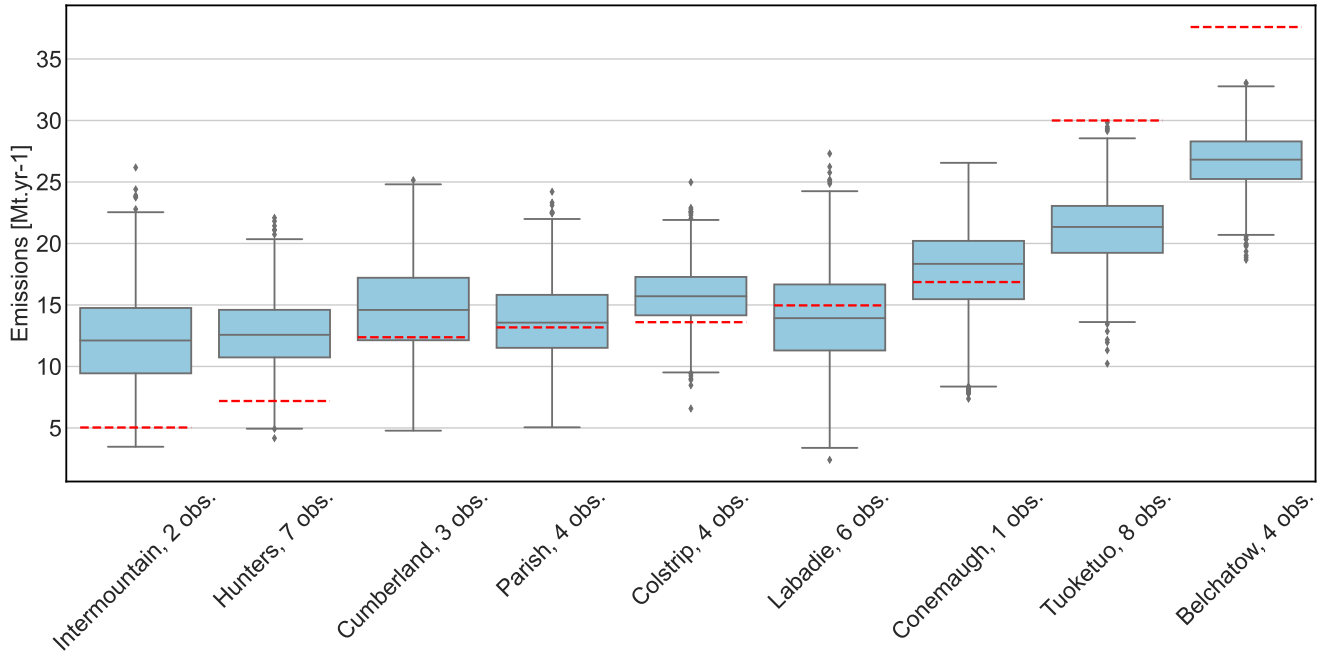


**Figure 8.** Boxplots of the ensembles of predictions based on the OCO-3 SAM observations for various power plants. Comparison with the reported annual emissions of the corresponding power plants (red dashed lines). Box spans the quartiles (25th to 75th percentiles), whiskers extend to the last points within  $1.5 \times \text{IQR}$  (interquartile range), and points beyond the whiskers represent outliers

2. An ensemble of 16 neural networks, all trained with slightly different hyperparameters considering various levels of cloud coverage, and either uniform or beta distribution used for augmentation.

Each neural network generates 100 predictions from the 100 images. The ensemble mean should give a more accurate estimate than a single prediction for  $x_i$  as seen with the synthetic data (see Section 4.1). Together with the 16 networks, we obtain 1600 predictions for each image, enhancing the robustness and reliability of our statistical analysis.

Figure 8 shows the ensemble of predictions for each power plant compared to the annual reported emissions.

The median absolute and median absolute relative differences between the ensemble average predictions and the reported emissions are  $7 \text{ Mt.yr}^{-1}$  and 29%, respectively. This relative difference of 29% is only slightly higher than what was observed on synthetic satellite imagery. Specifically, CNNs exhibit a good match with reported emissions for power plants with emissions ranging between  $10 \text{ Mt.yr}^{-1}$  and  $20 \text{ Mt.yr}^{-1}$  (e.g., Colstrip, Cumberland, Labadie, Parish, Conemaugh). However, the discrepancy with reported emissions largely increases for power plants at the extremes of low or high emissions (e.g., Belchatow, Tuocketuo, Hunters, Intermountain). The emissions estimated by the CNNs range from  $6.7 \text{ Mt.yr}^{-1}$  to  $30.4 \text{ Mt.yr}^{-1}$  (considering the 5% and 95% quantile predictions), whereas Belchatow's reported emissions stand at  $37.6 \text{ Mt.yr}^{-1}$  and Intermountain's at  $5 \text{ Mt.yr}^{-1}$ . This indicates that the variance in CNN predictions is significantly lower than that of the reported emissions. Given that the CNNs were trained on plumes with emission levels spanning from  $0 \text{ Mt.yr}^{-1}$  to  $45 \text{ Mt.yr}^{-1}$ , it was

initially anticipated that they could accurately predict plumes akin to those from Belchatow or Intermountain. Furthermore,  
275 in Section 4.1, we show that the CNNs reliably recover the low emissions ( $8.7 \text{ Mt.yr}^{-1}$  in average) of Turow power plant.  
The subsequent analyses will explore the causes of the observed discrepancies between extreme reported emissions and CNN  
predictions.

Figure 9 shows the predictions of a randomly selected CNN model from the ensemble for 8 specific OCO-3 SAM images.  
These images were chosen after a thorough inspection of all 39 snapshots in our dataset to illustrate the key patterns we identi-  
280 fied. For each OCO-3 SAM image, we show a sensitivity map obtained by the integrated gradient method, which computes the  
gradient of the model’s output (the emissions) relative to its input pixels, indicating how emissions are expected to increase or  
decrease with changes in pixel values. (see Dumont Le Brazidec et al. (2023) for details). Assuming that emissions estimates  
are directly correlated with the detection of plume pixels, the integrated gradient maps are anticipated to highlight a collection  
of positive pixels that effectively reconstruct the plume.

285 Images 9(a), 9(b), 9(c), and 9(d) are four instances of clear identification of the plume by the CNN. The integrated gradient  
method in each of these cases reveals collections of positive pixels forming a discernible plume shape. These positive pixels  
are encircled by negatives, suggesting that if the surrounding pixels intensified to match the plume’s pixel values, the CNN  
would less likely recognise these as plume pixels, interpreting the aggregate as elevated background values instead. Predictions  
closely match reported emissions in each scenario, barring the anomaly of Intermountain. This discrepancy is logical, given  
290 that the Intermountain plume is visually detectable in the image, whereas plumes corresponding to emissions of  $5 \text{ Mt.yr}^{-1}$  in  
the SMARTCARB dataset are typically obscured by the background.

Images 9(e) and 9(f) illustrate scenarios where clouds obscure the central portion of the image, thereby concealing a major  
part of the plume. These examples allow us to investigate how the CNN adapts to such conditions, making inferences based  
on the limited information available. In image 9(e), the CNN identifies a plume adjacent to the obscured area and bases its  
295 emissions estimate on this collection of pixels. In image 9(f), the CNN interprets a significant cluster of high-value pixels as  
the tail end of the concealed plume and calculates emissions based on this inferred section of the plume.

Images 9(g) and 9(h) shed light on a primary cause for the supposed overestimation of emissions from low-emitting power  
plants. These images feature barely discernible plumes alongside significant patterns (potentially systematic satellite errors)  
appearing on the left side of the images in both cases. The CNN mistakenly identifies these patterns as part of a plume in each  
300 case. Consequently, the model infers disproportionately high emissions based on this noise, leading to a substantial estimation  
of the emissions of these power plants.

In Figure 10, we propose a first possible explanation for the underestimation of high emission plumes by the CNN. Three  
observed high emission plumes—one from Belchatow and two from Tuoketuo—are compared against SMARTCARB plumes  
at the Belchatow or Tuoketuo reported emission levels. Specifically, the SMARTCARB simulations are chosen to represent  
305 emissions of  $37 \text{ Mt.yr}^{-1}$  and  $29.5 \text{ Mt.yr}^{-1}$ , aligning with the reported emissions for Belchatow and Tuoketuo, respectively,  
and have comparable ERA5 wind speeds to those at Belchatow or Tuoketuo snapshot OCO3-SAM images. The simulated  
plumes appear more pronounced against the background than their real counterparts, suggesting a higher emission magnitude.  
This observation might account for the model’s tendency to estimate lower emissions than Belchatow and Tuoketuo reported



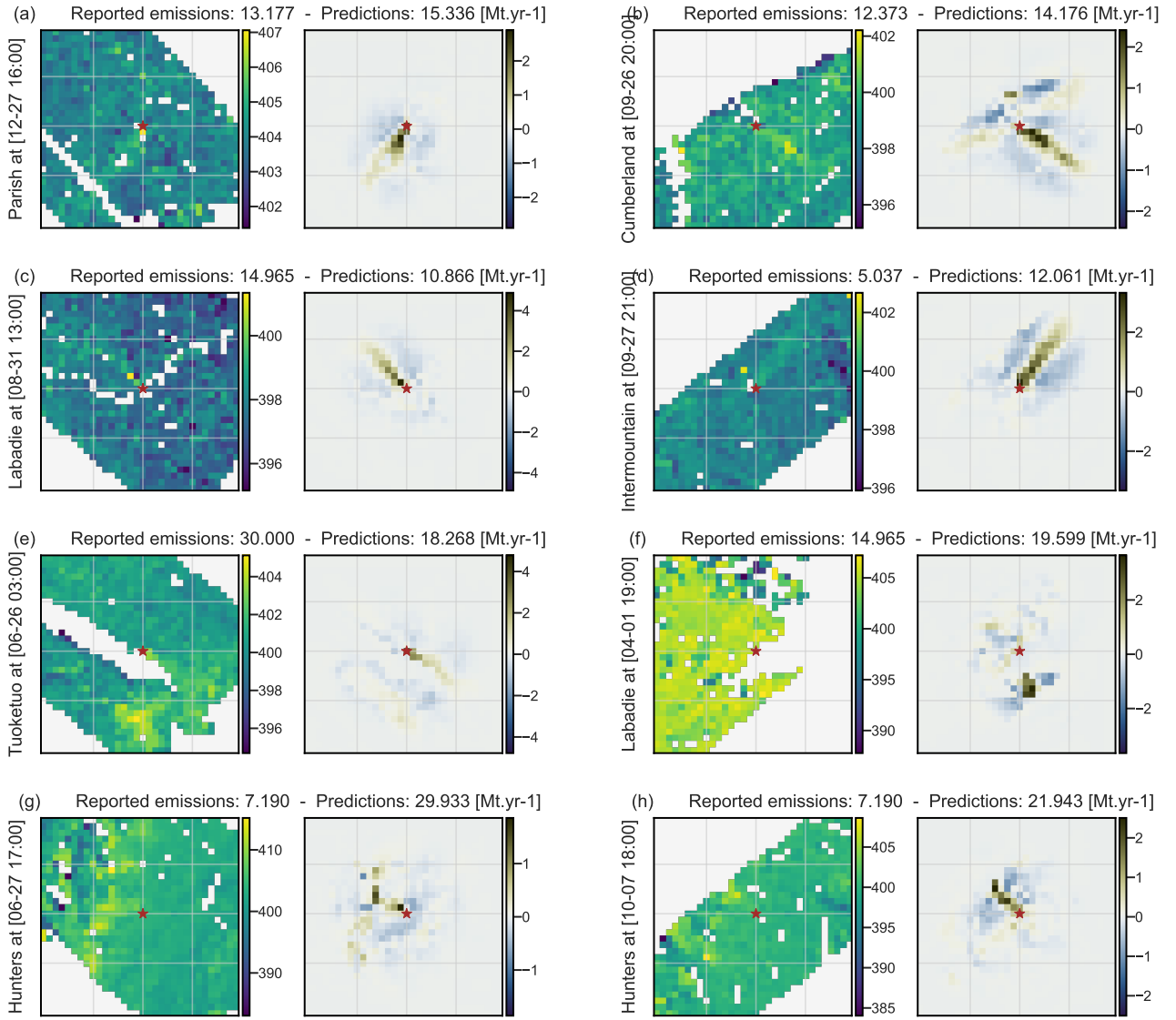
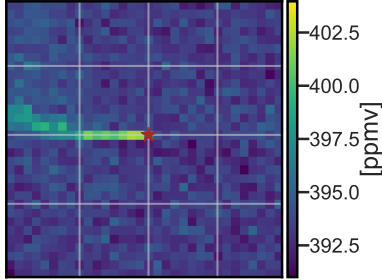
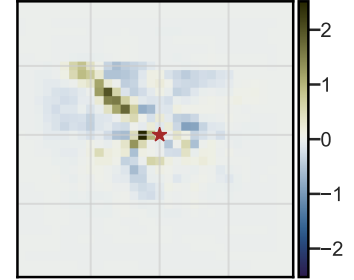
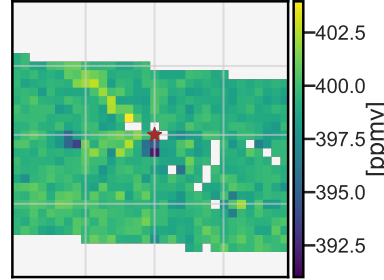


**Figure 9.** Analysis of the predictions of a CNN (chosen randomly from the ensemble) on 8 specific OCO-3 SAM images. Each of the image is presented alongside the resulting map (on its right) from the application of the integrated gradient method and the reported and predicted emissions in  $\text{Mt.yr}^{-1}$ . Power plant is indicated by a brown star. The  $\text{CO}_2$  concentration fields on the left are shown in ppmv. The integrated gradient images on the right represent dimensionless scores that indicate the contribution of each pixel to the predicted concentration.

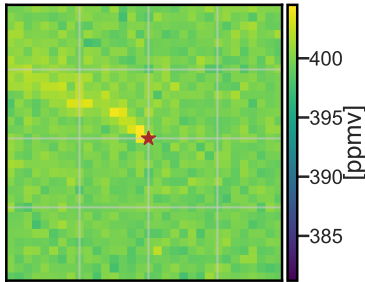
Sim. plume emissions = 37 Mt.yr-1



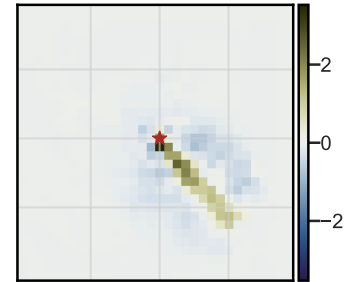
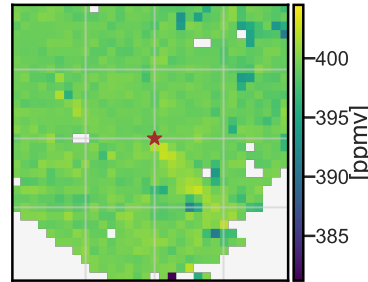
Belchatow at [06-24 07:00]



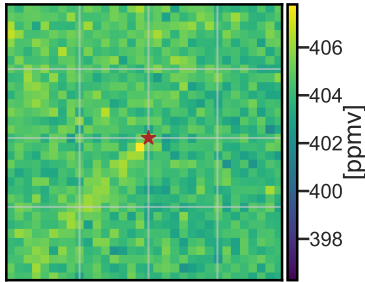
Sim. plume emissions = 30 Mt.yr-1



Tuoketuo at [06-18 06:00]



Sim. plume emissions = 30 Mt.yr-1



Tuoketuo at [10-16 00:00]

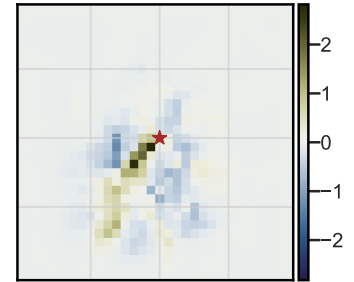
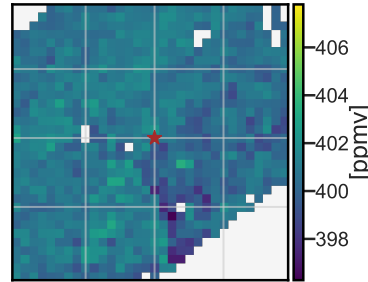


**Figure 10.** Analysis of the predictions of a CNN (chosen randomly from the ensemble) for 3 high emission plumes. One plume from Belchatow and two from Tuoketuo (middle column) are compared against equivalent high emission plumes from the SMARTCARB dataset (left column). For each OCO-3 SAM based plume, the integrated gradient approach is applied and presented on the right column. To ensure a fair comparison between columns 1 and 2, identical colorbars have been used. Power plant is indicated by a brown star.

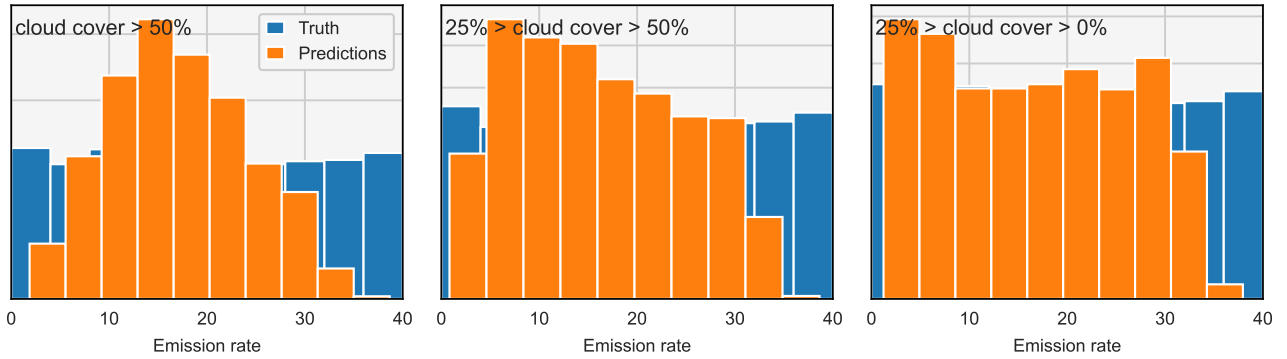


**Figure 11.** Distribution of the predictions of a CNN trained with uniformly distributed emissions, for synthetic images of the Dolna Odra power plant with uniformly distributed emissions, against the truth, at different levels of cloud coverage.

emissions. Further validation comes from the integrated gradient analysis, indicating accurate plume contour predictions by the model and affirming that the relevant information was used for its estimations.

Another reason for the CNN underestimating high emission plumes could be regression towards the mean in scenarios with high cloud levels. To show this, we train a CNN with a dataset of power plants with uniformly distributed emissions between 0 and 40 Mt.yr<sup>-1</sup> and a low cloud coverage (< 25% of the image covered with clouds). In Fig. 10, we plot the distribution of the predictions of the CNN for synthetic images of the Dolna Odra power plant with uniformly distributed emissions, against the truth, at different levels of cloud coverage. We observe a convergence to average values correlated with cloud coverage intensity. When the CNN lacks sufficient information in the image to infer emissions, it tends to average its predictions to minimise loss. A second observation is that even for low cloud coverage, the CNN struggles with emission levels higher than 33 Mt.yr<sup>-1</sup>, while it is trained with emissions uniformly distributed between 0 and 40 Mt.yr<sup>-1</sup> (note that the CNNs trained in previous sections were trained for emission levels between 0 and 45 Mt.yr<sup>-1</sup>). Increasing the number of high-emission plumes in the training dataset would likely reduce the CNN's bias towards emissions near the upper limit defined in the training data.

## 5 Discussions and limitations

The ability of CNNs to estimate CO<sub>2</sub> emissions from power plants plumes was validated on synthetic satellite images. The presence of cloud coverage does not significantly affect the CNNs performance, except in instances of substantial cloud presence. CNNs demonstrate adaptability, leveraging residual information to accurately estimate emissions under heavily clouded conditions. The inclusion of NO<sub>2</sub> data proves slightly beneficial, enhancing the CNN efficacy in all sky conditions.

Once trained on simulated XCO<sub>2</sub> images, the CNNs can be directly applied to real-world data with high accuracy, unlike traditional methods, which struggle to detect plumes and distinguish them from the background due to the low signal-to-noise ratio of CO<sub>2</sub> plumes. Nevertheless, it is observed that the spread of the CNN predictions is lower than the spread of the

OCO3-SAM reported emissions. Predictions are significantly higher for low-emission power plants due to the presence of systematic errors in the image that are falsely identified as plumes and significantly lower for high-emission power plants. Furthermore, predictions are lower than reported annual emissions for high-emission power plants. This is likely due to regression towards the mean in weakly informative images and/or discrepancies between the training and evaluation datasets. Finally, it is acknowledged that comparing instantaneous emissions measured during satellite overpasses with reports of annual average emissions from the EPA and E-PRTR inventories presents challenges, owing to the variability and intermittent nature of power production and CO<sub>2</sub> emissions.

The divergence between the distributions of real XCO<sub>2</sub> observations and those of the simulations observed in Section 4.2, particularly in terms of systematic satellite errors, creates a domain shift between training and test conditions that likely leads to systematic errors in CNN predictions, necessitating CNN adaptation. To account for systematic satellite errors, a promising approach involves mingling real and simulated data during the training phase, such as overlaying a simulated plume of known emissions onto a real background. This method would introduce systematic errors typical of real satellite data while maintaining a controlled environment for supervised learning.

## 6 Conclusions and perspectives

In this paper, we improve the CNN model for the inversion of CO<sub>2</sub> plumes from Dumont Le Brazidec et al. (2023) through the introduction of a novel data augmentation strategy and a dedicated approach to deal with clouds. This methodology was validated using the synthetic CO2M observations from the SMARTCARB dataset, demonstrating its efficacy in handling cloud-covered scenarios. Our findings indicate that, on average, clouds do not pose a significant challenge for CNNs, which maintain high performance levels under both sparse and dense cloud conditions. An exception is observed in the case of the Turow power plant, where performance significantly drops. This decline is likely attributable to Turow’s relatively low emission levels, which results in its plumes being inherently less distinguishable from the background.

Following its validation, the methodology is applied to OCO-3 SAM observations. In total 39 observations across 9 power plants, adjusted for resolution and shape to match CNN input requirements, are analysed. For each observation, an ensemble of predictions is produced by CNNs trained on the SMARTCARB synthetic dataset. The results are promising, exhibiting a relative difference with the reported emissions only slightly superior to the relative error observed with the synthetic dataset. Specifically, predicted emissions for images from mid-level emission power plants, such as Colstrip and Parish, correspond very accurately to reported emissions. Moreover, through the application of integrated gradient techniques, it is demonstrated that the CNNs effectively identify plumes in the OCO-3 SAM images and accurately estimate emissions from the plumes’ physical locations.

However, we observed that images capturing low and high emission power plants plumes are prone to overestimation and underestimation, respectively, in comparison to the reported emissions. Systematic satellite retrieval errors are identified as a frequent cause of overestimation in the low emission power plant images. These errors, often non-Gaussian and absent in the synthetic training dataset, lead to significant inaccuracies.

This study demonstrates the feasibility of applying neural networks to real satellite imagery of XCO<sub>2</sub> following training on simulated datasets. Although we advocate the integration of a hybrid training approach that incorporates both real and simulated images in order to improve the robustness and accuracy of the model, we provide a ready-to-use CNN CO<sub>2</sub> plume inversion tool based on satellite imagery.

*Data availability.* The datasets used in this paper are available on a compliant repository on <https://doi.org/10.5281/zenodo.12788520> and originate from <https://zenodo.org/record/4048228>. The weights of the CNNs are available on <https://doi.org/10.5281/zenodo.12788520>. The codes for training the CNN are available on <https://doi.org/10.5281/zenodo.14013176>.

*Author contributions.* JDLB contributed to conceptualisation, developed the methodology, implemented the software, conducted the investigation, performed formal analysis, created the visualisations, managed resources, and administered the project. PV contributed to the investigation and formal analysis. AF contributed to conceptualisation, methodology, and project administration. MB contributed to the conceptualisation, methodology, administered the project and secured funding. GB contributed to conceptualisation and methodology. GK provided resources. JDLB wrote the original draft with GB, GK, AF, MB, and PV contributing by reviewing it.

*Competing interests.* The authors declare that they have no conflict of interest.

*Acknowledgements.* This project has been funded by the European Union's Horizon 2020 research and innovation programme under grant agreement N° 958927 (Prototype system for a Copernicus CO<sub>2</sub> service). CEREIA is a member of Institut Pierre-Simon Laplace (IPSL). Thanks to Robert R. Nelson for his assistance with downloading the OCO-3 SAM images.

## References

- Broquet, G., Bréon, F.-M., Renault, E., Buchwitz, M., Reuter, M., Bovensmann, H., Chevallier, F., Wu, L., and Ciais, P.: The potential of satellite spectro-imagery for monitoring CO<sub>2</sub> emissions from large cities, *Atmospheric Measurement Techniques*, 11, 681–708, <https://doi.org/10.5194/amt-11-681-2018>, publisher: Copernicus GmbH, 2018.
- Brunner, D., Kuhlmann, G., Marshall, J., Clément, V., Fuhrer, O., Broquet, G., Löscher, A., and Meijer, Y.: Accounting for the vertical distribution of emissions in atmospheric CO<sub>2</sub> simulations, *Atmos Chem Phys*, 19, 4541–4559, <https://doi.org/10.5194/acp-19-4541-2019>, publisher: Copernicus GmbH, 2019.
- Chevallier, F., Remaud, M., O'Dell, C. W., Baker, D., Peylin, P., and Cozic, A.: Objective evaluation of surface- and satellite-driven carbon dioxide atmospheric inversions, *Atmospheric Chemistry and Physics*, 19, 14 233–14 251, <https://doi.org/10.5194/acp-19-14233-2019>, publisher: Copernicus GmbH, 2019.
- Chevallier, F., Broquet, G., Zheng, B., Ciais, P., and Eldering, A.: Large CO<sub>2</sub> Emitters as Seen From Satellite: Comparison to a Gridded Global Emission Inventory, *Geophysical Research Letters*, 49, e2021GL097 540, <https://doi.org/10.1029/2021GL097540>, <https://onlinelibrary.wiley.com/doi/pdf/10.1029/2021GL097540>, 2022.
- Cusworth, D. H., Duren, R. M., Thorpe, A. K., Eastwood, M. L., Green, R. O., Dennison, P. E., Frankenberg, C., Heckler, J. W., Asner, G. P., and Miller, C. E.: Quantifying Global Power Plant Carbon Dioxide Emissions With Imaging Spectroscopy, *AGU Advances*, 2, e2020AV000 350, <https://doi.org/10.1029/2020AV000350>, <https://onlinelibrary.wiley.com/doi/pdf/10.1029/2020AV000350>, 2021.
- Danjou, A., Broquet, G., Schuh, A., Bréon, F.-M., and Lauvaux, T.: Optimal selection of satellite XCO<sub>2</sub> images over cities for urban CO<sub>2</sub> emission monitoring using a global adaptive-mesh model, *Atmospheric Measurement Techniques Discussions*, pp. 1–33, <https://doi.org/10.5194/amt-2023-199>, publisher: Copernicus GmbH, 2023.
- Danjou, A., Broquet, G., Lian, J., Bréon, F.-M., and Lauvaux, T.: Evaluation of light atmospheric plume inversion methods using synthetic XCO<sub>2</sub> satellite images to compute Paris CO<sub>2</sub> emissions, *Remote Sensing of Environment*, 305, 113 900, <https://doi.org/10.1016/j.rse.2023.113900>, 2024.
- Dumont Le Brazidec, J., Vanderbecken, P., Farchi, A., Bocquet, M., Lian, J., Broquet, G., Kuhlmann, G., Danjou, A., and Lauvaux, T.: Segmentation of XCO<sub>2</sub> images with deep learning: application to synthetic plumes from cities and power plants, *Geoscientific Model Development Discussions*, pp. 1–29, <https://doi.org/10.5194/gmd-2022-288>, publisher: Copernicus GmbH, 2022.
- Dumont Le Brazidec, J., Vanderbecken, P., Farchi, A., Broquet, G., Kuhlmann, G., and Bocquet, M.: Deep learning applied to CO<sub>2</sub> power plant emissions quantification using simulated satellite images, *Geoscientific Model Development Discussions*, pp. 1–30, <https://doi.org/10.5194/gmd-2023-142>, publisher: Copernicus GmbH, 2023.
- Eldering, A., Taylor, T. E., O'Dell, C. W., and Pavlick, R.: The OCO-3 mission: measurement objectives and expected performance based on 1 year of simulated data, *Atmospheric Measurement Techniques*, 12, 2341–2370, <https://doi.org/10.5194/amt-12-2341-2019>, publisher: Copernicus GmbH, 2019.
- Finch, D., Palmer, P., and Zhang, T.: Automated detection of atmospheric NO<sub>2</sub> plumes from satellite data: a tool to help infer anthropogenic combustion emissions, *Atmos. Meas. Tech.*, pp. 1–21, <https://doi.org/10.5194/amt-2021-177>, 2021.
- Grant, D., Zelinka, D., and Mitova, S.: Reducing CO<sub>2</sub> emissions by targeting the world's hyper-polluting power plants\*, *Environmental Research Letters*, 16, 094 022, <https://doi.org/10.1088/1748-9326/ac13f1>, publisher: IOP Publishing, 2021.

- 415 Hakkarainen, J., Szélag, M. E., Ialongo, I., Retscher, C., Oda, T., and Crisp, D.: Analyzing nitrogen oxides to carbon dioxide emission ratios from space: A case study of Matimba Power Station in South Africa, *Atmospheric Environment: X*, 10, 100110, <https://doi.org/10.1016/j.aeaoa.2021.100110>, 2021.
- Hakkarainen, J., Kuhlmann, G., Koene, E., Santaren, D., Meier, S., Krol, M. C., van Stratum, B. J. H., Ialongo, I., Chevallier, F., Tamminen, J., Brunner, D., and Broquet, G.: Analyzing nitrogen dioxide to nitrogen oxide scaling factors for data-driven satellite-based emission  
420 estimation methods: A case study of Matimba/Medupi power stations in South Africa, *Atmospheric Pollution Research*, 15, 102171, <https://doi.org/10.1016/j.apr.2024.102171>, 2024.
- Janssens-Maenhout, G., Pinty, B., Dowell, M., Zunker, H., Andersson, E., Balsamo, G., Bézy, J.-L., Brunhes, T., Bösch, H., Bojkov, B., Brunner, D., Buchwitz, M., Crisp, D., Ciais, P., Counet, P., Dee, D., Gon, H. D. v. d., Dolman, H., Drinkwater, M. R., Dubovik, O., Engelen, R., Fehr, T., Fernandez, V., Heimann, M., Holmlund, K., Houweling, S., Husband, R., Juvyns, O., Kentarchos, A., Landgraf, J.,  
425 Lang, R., Löscher, A., Marshall, J., Meijer, Y., Nakajima, M., Palmer, P. I., Peylin, P., Rayner, P., Scholze, M., Sierk, B., Tamminen, J., and Veeffkind, P.: Toward an Operational Anthropogenic CO<sub>2</sub> Emissions Monitoring and Verification Support Capacity, *Bulletin of the American Meteorological Society*, 101, E1439–E1451, <https://doi.org/10.1175/BAMS-D-19-0017.1>, publisher: American Meteorological Society Section: Bulletin of the American Meteorological Society, 2020.
- Jongaramrungruang, S., Matheou, G., Thorpe, A. K., Zeng, Z.-C., and Frankenberg, C.: Remote sensing of methane plumes: instrument  
430 tradeoff analysis for detecting and quantifying local sources at global scale, *Atmospheric Measurement Techniques*, 14, 7999–8017, <https://doi.org/10.5194/amt-14-7999-2021>, publisher: Copernicus GmbH, 2021.
- Joyce, P., Ruiz Villena, C., Huang, Y., Webb, A., Gloor, M., Wagner, F. H., Chipperfield, M. P., Barrio Guilló, R., Wilson, C., and Boesch, H.: Using a deep neural network to detect methane point sources and quantify emissions from PRISMA hyperspectral satellite images, *Atmospheric Measurement Techniques*, 16, 2627–2640, <https://doi.org/10.5194/amt-16-2627-2023>, publisher: Copernicus GmbH, 2023.
- 435 Kuhlmann, G., Broquet, G., Marshall, J., Clément, V., Löscher, A., Meijer, Y., and Brunner, D.: Detectability of CO<sub>2</sub> emission plumes of cities and power plants with the Copernicus Anthropogenic CO<sub>2</sub> Monitoring (CO<sub>2</sub>M) mission, *Atmos. Meas. Tech.*, 12, 6695–6719, <https://doi.org/10.5194/amt-12-6695-2019>, 2019.
- Kuhlmann, G., Brunner, D., Broquet, G., and Meijer, Y.: Quantifying CO<sub>2</sub> emissions of a city with the Copernicus Anthropogenic CO<sub>2</sub> Monitoring satellite mission, *Atmos. Meas. Tech.*, 13, 6733–6754, <https://doi.org/10.5194/amt-13-6733-2020>, 2020.
- 440 Kuhlmann, G., Henne, S., Meijer, Y., and Brunner, D.: Quantifying CO<sub>2</sub> Emissions of Power Plants With CO<sub>2</sub> and NO<sub>2</sub> Imaging Satellites, *Front. remote sens.*, 2, <https://www.frontiersin.org/article/10.3389/frsen.2021.689838>, 2021.
- Kuhlmann, G., Koene, E. F. M., Meier, S., Santaren, D., Broquet, G., Chevallier, F., Hakkarainen, J., Nurmela, J., Amorós, L., Tamminen, J., and Brunner, D.: The `ddeq` Python library for point source quantification from remote sensing images (Version 1.0), *EGUsphere*, pp. 1–27, <https://doi.org/10.5194/egusphere-2023-2936>, publisher: Copernicus GmbH, 2024.
- 445 Kumar, S., Arevalo, I., Iftekhar, A. S. M., and Manjunath, B. S.: MethaneMapper: Spectral Absorption Aware Hyperspectral Transformer for Methane Detection, pp. 17 609–17 618, [https://openaccess.thecvf.com/content/CVPR2023/html/Kumar\\_MethaneMapper\\_Spectral\\_Absorption\\_Aware\\_Hyperspectral\\_Transformer\\_for\\_Methane\\_Detection\\_CVPR\\_2023\\_paper.html](https://openaccess.thecvf.com/content/CVPR2023/html/Kumar_MethaneMapper_Spectral_Absorption_Aware_Hyperspectral_Transformer_for_Methane_Detection_CVPR_2023_paper.html), 2023.
- Lary, D. J., Alavi, A. H., Gandomi, A. H., and Walker, A. L.: Machine learning in geosciences and remote sensing, *Geoscience Frontiers*, 7, 3–10, <https://doi.org/10.1016/j.gsf.2015.07.003>, 2016.
- 450 Lin, X., van der A, R., de Laat, J., Eskes, H., Chevallier, F., Ciais, P., Deng, Z., Geng, Y., Song, X., Ni, X., Huo, D., Dou, X., and Liu, Z.: Monitoring and quantifying CO<sub>2</sub> emissions of isolated power plants from space, *Atmospheric Chemistry and Physics*, 23, 6599–6611, <https://doi.org/10.5194/acp-23-6599-2023>, publisher: Copernicus GmbH, 2023.

- Meijer, Y.: Copernicus CO<sub>2</sub> Monitoring Mission Requirements Document, Earth and Mission Science Division, 84, [https://esamultimedia.esa.int/docs/EarthObservation/CO2M\\_MRD\\_v3.0\\_20201001\\_Issued.pdf](https://esamultimedia.esa.int/docs/EarthObservation/CO2M_MRD_v3.0_20201001_Issued.pdf), 2020.
- 455 Meijer, Y., Andersson, E., Boesch, H., Dubovik, O., Houweling, S., Landgraf, J., Lang, R., and Lindqvist, H.: Editorial: Anthropogenic emission monitoring with the Copernicus CO<sub>2</sub> monitoring mission, *Frontiers in Remote Sensing*, 4, <https://doi.org/10.3389/frsen.2023.1217568>, publisher: Frontiers, 2023.
- Nassar, R., Hill, T. G., McLinden, C. A., Wunch, D., Jones, D. B. A., and Crisp, D.: Quantifying CO<sub>2</sub> Emissions From Individual Power Plants From Space, *Geophysical Research Letters*, 44, 10,045–10,053, <https://doi.org/10.1002/2017GL074702>, \_eprint: <https://onlinelibrary.wiley.com/doi/pdf/10.1002/2017GL074702>, 2017.
- 460 Nassar, R., Mastrogiacomo, J.-P., Bateman-Hemphill, W., McCracken, C., MacDonald, C. G., Hill, T., O'Dell, C. W., Kiel, M., and Crisp, D.: Advances in quantifying power plant CO<sub>2</sub> emissions with OCO-2, *Remote Sensing of Environment*, 264, 112579, <https://doi.org/10.1016/j.rse.2021.112579>, 2021.
- Nassar, R., Moeini, O., Mastrogiacomo, J.-P., O'Dell, C. W., Nelson, R. R., Kiel, M., Chatterjee, A., Eldering, A., and Crisp, D.: Tracking CO<sub>2</sub> emission reductions from space: A case study at Europe's largest fossil fuel power plant, *Frontiers in Remote Sensing*, 3, <https://www.frontiersin.org/articles/10.3389/frsen.2022.1028240>, 2022.
- 465 Pillai, D., Buchwitz, M., Gerbig, C., Koch, T., Reuter, M., Bovensmann, H., Marshall, J., and Burrows, J. P.: Tracking city CO<sub>2</sub> emissions from space using a high-resolution inverse modelling approach: a case study for Berlin, Germany, *Atmospheric Chemistry and Physics*, 16, 9591–9610, <https://doi.org/10.5194/acp-16-9591-2016>, publisher: Copernicus GmbH, 2016.
- 470 Reuter, M., Buchwitz, M., Schneising, O., Krautwurst, S., O'Dell, C. W., Richter, A., Bovensmann, H., and Burrows, J. P.: Towards monitoring localized CO<sub>2</sub> emissions from space: co-located regional CO<sub>2</sub> and NO<sub>2</sub> enhancements observed by the OCO-2 and S5P satellites, *Atmos Chem Phys*, 19, 9371–9383, <https://doi.org/10.5194/acp-19-9371-2019>, 2019.
- Santaren, D., Hakkarainen, J., Kuhlmann, G., Koene, E., Chevallier, F., Ialongo, I., Lindqvist, H., Nurmela, J., Tamminen, J., Amoros, L., Brunner, D., and Broquet, G.: Benchmarking data-driven inversion methods for the estimation of local CO<sub>2</sub> emissions from XCO<sub>2</sub> and NO<sub>2</sub> satellite images, *Atmospheric Measurement Techniques Discussions*, pp. 1–52, <https://doi.org/10.5194/amt-2023-241>, publisher: Copernicus GmbH, 2024.
- 475 Taylor, T. E., O'Dell, C. W., Baker, D., Bruegge, C., Chang, A., Chapsky, L., Chatterjee, A., Cheng, C., Chevallier, F., Crisp, D., Dang, L., Drouin, B., Eldering, A., Feng, L., Fisher, B., Fu, D., Gunson, M., Haemmerle, V., Keller, G. R., Kiel, M., Kuai, L., Kurosu, T., Lambert, A., Laughner, J., Lee, R., Liu, J., Mandrake, L., Marchetti, Y., McGarragh, G., Merrelli, A., Nelson, R. R., Osterman, G., Oyafuso, F., Palmer, P. I., Payne, V. H., Rosenberg, R., Somkuti, P., Spiers, G., To, C., Weir, B., Wennberg, P. O., Yu, S., and Zong, J.: Evaluating the consistency between OCO-2 and OCO-3 XCO<sub>2</sub> estimates derived from the NASA ACOS version 10 retrieval algorithm, *Atmospheric Measurement Techniques*, 16, 3173–3209, <https://doi.org/10.5194/amt-16-3173-2023>, publisher: Copernicus GmbH, 2023.
- 480 Varon, D. J., Jacob, D. J., McKeever, J., Jervis, D., Durak, B. O. A., Xia, Y., and Huang, Y.: Quantifying methane point sources from fine-scale satellite observations of atmospheric methane plumes, *Atmospheric Measurement Techniques*, 11, 5673–5686, <https://doi.org/10.5194/amt-11-5673-2018>, publisher: Copernicus GmbH, 2018.
- Wu, D., Lin, J. C., Oda, T., and Kort, E. A.: Space-based quantification of per capita CO<sub>2</sub> emissions from cities, *Environmental Research Letters*, 15, 035 004, <https://doi.org/10.1088/1748-9326/ab68eb>, publisher: IOP Publishing, 2020.
- Zheng, B., Chevallier, F., Ciais, P., Broquet, G., Wang, Y., Lian, J., and Zhao, Y.: Observing carbon dioxide emissions over China's cities and industrial areas with the Orbiting Carbon Observatory-2, *Atmospheric Chemistry and Physics*, 20, 8501–8510, <https://doi.org/10.5194/acp-20-8501-2020>, publisher: Copernicus GmbH, 2020.
- 490